Inorganic Chemistry

Article

pubs.acs.org/IC

Anion−π and Halide−Halide Nonbonding Interactions in a New Ionic Liquid Based on Imidazolium Cation with Three-Dimensional Magnetic Ordering in the Solid State

Abel García-Saiz,[†] Imanol de Pedro,*[,†] Pedro Migowski,[‡] Oriol Vallcorba,[§] Javier Junquera,[†] Jesús Angel Blanco,[⊥] Oscar Fabelo,[∥] Denis Sheptyakov,[⊗] Joao Carlos Waerenborgh,[▽] María Teresa Fernández-Díaz,[∥] Jordi Rius,[§] Jairton Dupont,[‡] Jesús Antonio Gonzalez,[†] and Jesús Rodríguez Fernández[†]

[†]CITIMAC, Facultad de Ciencias, Universidad de Cantabria, 39005 Santander, Spain

[‡]Universidade Federal do Rio Grande do Sul, 90040-060 Porto Alegre, Brazil

[§]Institut de Ciència de Materials de Barcelona (CSIC) Campus de la UAB, 08193 Bellaterra, Catalunya, Spain

[⊥]Departamento de Física, Universidad de Oviedo, 33007 Oviedo, Spain

[∥]Institut Laue-Langevin, BP 156X, F-38042 Grenoble Cedex, France

[⊗]Laboratory for Neutron Scattering and Imaging, Paul Scherrer Institut, 5232 Villigen PSI, Villigen, Switzerland

[▽]Centro de Ciências e Tecnologias Nucleares, Instituto Superior Técnico, Universidade de Lisboa, CFMC-UL, 2695-066 Bobadela LRS, Portugal

Supporting Information

ABSTRACT: We present the first magnetic phase of an ionic liquid with anion−π interactions, which displays a three-dimensional (3D) magnetic ordering below the Néel temperature, T_N = 7.7 K. In this material, called Dimim[$FeBr_4$], an exhaustive and systematic study involving structural and physical characterization (synchrotron X-ray, neutron powder diffraction, direct current and alternating current magnetic susceptibility, magnetization, heat capacity, Raman and Mössbauer measurements) as well as first-principles analysis (density functional theory (DFT) simulation) was performed.

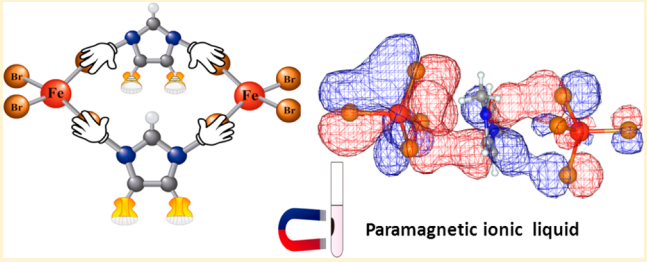

The crystal structure, solved by Patterson-function direct methods, reveals a monoclinic phase ($P2_1$ symmetry) at room temperature with a = 6.745(3) Å, b = 14.364(3) Å, c = 6.759(3) Å, and β = 90.80(2)°. Its framework, projected along the b direction, is characterized by layers of cations [Dimim]$^+$ and anions [$FeBr_4$]$^-$ that change the orientation from layer to layer, with Fe···Fe distances larger than 6.7 Å. Magnetization measurements show the presence of 3D antiferromagnetic ordering below T_N with the existence of a noticeable magneto−crystalline anisotropy. From low-temperature neutron diffraction data, it can be observed that the existence of antiferromagnetic order is originated by the antiparallel ordering of ferromagnetic layers of [$FeBr_4$]$^-$ metal complex along the b direction. The magnetic unit cell is the same as the chemical one, and the magnetic moments are aligned along the c direction. The DFT calculations reflect the fact that the spin density of the iron ions spreads over the bromine atoms. In addition, the projected density of states (PDOS) of the imidazolium with the bromines of a [$FeBr_4$]$^-$ metal complex confirms the existence of the anion−π interaction. Magneto−structural correlations give no evidence for direct iron−iron interactions, corroborating that the 3D magnetic ordering takes place via superexchange coupling, the Fe−Br···Br−Fe interplane interaction being defined as the main exchange pathway.

1. INTRODUCTION

Hybrid organic−inorganic materials now play the major role in the development of advanced functional materials.[1] Research in these materials is supported by the growing interest of chemists, physicists, biologists, and materials scientists due to the opportunity to combine useful properties of both components (organic and inorganic) and the possibility of tuning the physical properties thanks to small modifications at the interface.[2] A new class of these materials are the magnetic ionic liquids (MILs), where the organic and inorganic constituents are embedded, and only hydrogen, van der Waals (vdw), and/or ionic bonds provide cohesion between them.[3] These metal-containing ionic liquids combine the properties of ionic liquids, defined as salts with the melting point below 100 °C,[4] with additional intrinsic magnetic,[5]

Received: April 16, 2014
Published: July 31, 2014

   dx.doi.org/10.1021/ic500882z | Inorg. Chem. 2014, 53, 8384−8396

spectroscopic,[6] or catalytic[7] properties depending on the enclosed metal ion used. Thus, in the past few years, the synthesis, study, and application of these smart materials have increased exponentially.[8] First, MILs were composed of a metal-containing anion (such as iron, cobalt, manganese, copper) and an organic cation, generally imidazolium, pyrrolidinium, pyridinium,[9] or tetraalkylphosphonium.[10] In more recent years, the development of these materials has made possible the combination of different rare-earth ions (neodymium, gadolinium, dysprosium),[11] chiral amionacids,[12] bimagnetic ions,[13] or heteroanions[5] to increase or improve their technological applications, such as the transport and separation of materials,[14] separation of greenhouse gases (CO_2) through supported MILs membranes,[15] magnetic surfactants,[5] esterification of acid oleic to biodiesel,[16] etc.

The noncovalent interactions play the most important role in the organization of the structural units of MILs.[17] A good understanding of these interactions would give rise to the improvement of their technological applications. Many research groups have focused upon understanding the Coulomb, dipole−dipole, and hydrogen bonds within the crystal structures of these compounds.[18] However, in MILs based on halometallates[19] MX_4 (M = metal and X = halogen), such as the compound studied in this work, namely, the 1,3-dimethylimidazolium tetrabromoferrate Dimim[$FeBr_4$], it is necessary to consider other nonbonding interactions, such as halogen−halogen[20] (between two bromine atoms of two neighboring $[FeBr_4]^-$ tetrahedra) or anion−π[21] (between $[FeBr_4]^-$ anion and imidazolium cation), because these also contribute to the molecular self-assembly of the anion species in the crystal framework.[22] In addition, these noncovalent interactions develop very interesting electrical and magnetic phenomena; for instance, in hybrid organic−inorganic materials based on the halopyridinium metal complex $(4\text{-XpyH})_2[CoX_4]$ (X = Cl or Br and pyH = 4-halopyridinium),[23] in the magnetic conducting molecular system of BEDT-TTF and BETS, based on tetrahalometallate[24] $(DMET)_2FeBr_4$, $(EDTDM)_2FeBr_4$ or $(EDOTTFBr_2)_2FeX_4$ (X = Cl and Br),[25] where the electron transport and magnetism (antiferromagnetism with a weak ferromagnetism) interplay, or in the family of MILs based on imidazolium and tetrachloroferrate ions,[26] where the Fe−Cl···Cl−Fe noncovalent interactions are strong enough for the establishment of a three-dimensional (3D) magnetic ordering.

In previous works we have shown that (i) halogen−halogen interactions may serve as a primary force that induces a 3D magnetic ordering in MILs based on imidazolium and tetrachloroferrate ions,[27] (ii) the spin population in the metal complex anion and the distances and angles between the superexchange pathways of the type Fe−X···X−Fe (X = halide) play a decisive role in the formation and stability of these 3D magnetic orderings, and (iii) a smaller chain length of the organic cation increases the efficiency in the transmission of the magnetic interactions, resulting in an increase in the ordering temperatures [from $[Bmim]^+$[28] that shows no 3D magnetic ordering through $[Emim]^+$ (T_N = 4 K)[26] to $[Dimim]^+$ (T_N = 5.6 K)[29]] (Bmim = 1-butyl-3-methylimidazolium; Emim = 1-ethyl-3-methylimidazolium). In the present study we substituted the chloride ion in the metal complex by a less electronegative halide ion, bromide, based on the principles that the magnetic interaction between the $[FeX_4]^-$ anion should be stronger in the order X = I > Br > Cl > F. This replacement would allow a larger delocalization of the charge density in the metal complex anion $[FeBr_4]$ than in the related $[FeCl_4]$, which will favor both the formation of stronger halogen−halogen interactions and the arrangement of anion−π interactions with the imidazolium cation. In fact, it has been found that the replacement of Cl with Br in Emim[FeX_4][26b] leads to an increase in the Neel temperature. Herein we report the synthesis and physicochemical characterization of a new MIL, namely, Dimim[$FeBr_4$]. The magneto−structural study involving experimental results and density functional theory (DFT) calculations will be also presented.

2. EXPERIMENTAL SECTION

The synthesis of Dimim[$FeBr_4$] was realized following a method previously used for Dimim[$FeCl_4$].[29] For the chemical characterization, elemental and thermal analyses were used. The crystal and magnetic structures were obtained by synchrotron X-ray powder diffraction and by high- and low-resolution neutron diffraction experiments. The physical characterization was studied using direct current (DC) and alternating current (AC) magnetic susceptibility, magnetization, heat capacity, Raman, and Mössbauer measurements. Finally, density functional first-principles simulations based on a numerical atomic orbital method as implemented in the SIESTA[30] code were carried out. All the calculations were performed within the efficient implementation[31] of the vdw density functional of Dion et al.,[32] recently tested on imidazolium-based ionic liquids.[33] For a more detailed description of the Experimental Section, see the Supporting Information.

3. RESULTS AND DISCUSSION

3.1. Description of the Crystal Structure. The crystal structure of Dimim[$FeBr_4$] at 280 and 300 K, listed in the Supporting Information and the corresponding CIF files, were solved from synchrotron X-ray powder diffraction (SXPD) and high-resolution neutron diffraction data, respectively. The indexing of the patterns showed similar unit cell parameters and the same space group ($P2_1$) as the reported structure for Dimim[$FeCl_4$][29] at room temperature, which was used as the starting model for the Rietveld refinements. Neutron data had enough quality to locate the hydrogen atoms in the crystal structure but not to refine the CH bond lengths. To improve the refinement, the crystal structure was optimized by DFT calculations, using the output of the initial neutron Rietveld refinement as the initial position of the theoretical conjugate gradient minimization. With the coordinates from the initial Rietveld refinement and soft distance restraints obtained from the DFT model, a final crystal refinement of both sets of data of Dimim[$FeBr_4$], at 280 and 300 K, was performed. Both crystal structures obtained are practically equivalent, with only a slight variation in the $[Dimim]^+$ cation orientation. The experimental, calculated, and difference powder diffraction profiles are shown in Figure S.2 of Supporting Information. The final structural parameters and figures of merit of the last refinements are summarized in Table S.2 and the positional parameters are given in Table S.3 of the Supporting Information. For the structural discussion, the crystal structure at 300 K (neutron data) will be taken due to the better determination of H positions (with synchrotron data H atoms are constrained to the respective C atoms). The most relevant interatomic distances in Dimim[$FeBr_4$] crystal structure at 300 K are displayed in Table 1.

The crystal structure of Dimim[$FeBr_4$] at 300 K can be defined as layers of $[Dimim]^+$ cations and $[FeBr_4]^-$ anions stacked along the *b* direction with Fe···Fe distances of 6.74(4) and 6.76(3) Å inside a layer (in the *a* and *c* directions) and 8.57(1) Å between the layers (the *b* direction) (see Figure 1).

dx.doi.org/10.1021/ic500882z | Inorg. Chem. 2014, 53, 8384−8396

Table 1. Most Relevant Interatomic Distances in Dimim[$FeBr_4$] Crystal Structure at 300 and 0 K Obtained from HRPT and DFT, Respectively

	HRPT, 300 K		DFT, 0 K	
	length (Å)	angle (deg)	length (Å)	angle (deg)
Br···Br				
Br1···Br3	3.69(7)		4.108	
Br3···Br4	3.71(7)		3.913	
Br2···Br3	3.83(5)		4.284	
H···Br (potential hydrogen bonds)				
C4−H4···Br1	2.67(5)	160(3)	3.011	173.4
C5−H5···Br3	2.89(8)	119(5)	3.061	121.9
C1′−H1B′···Br3	2.89(7)	133(5)	3.131	150.7
C1′−H1B′···Br1	3.06(8)	119(2)	3.318	128(1)
C1′−H1A′···Br4	3.10(4)	120(3)	3.477	101.9
C1′−H1C′···Br2	3.00(10)	99(3)[a]	3.553	97.4
C1″−H1B″···Br2	3.01(9)	154(4)	3.612	116.9
C2−H2···Br1	3.20(5)[b]	167(4)	3.227	155.2
[FeBr]⁻···[Dimim]⁺ (potential π−d interactions)				
Fe···Centroid	4.32(2)	87.6[c]	4.598	76.2
Br2···C5	3.38(3)		3.878	
Br4···N1	3.69(5)		4.111	
Br4···[N1−C2][d]	3.67(5)		4.056	
Br3···N3	3.93(5)		3.929	
Br1···Centroid	6.75(5)	85.3	7.010	78.8
Br2···Centroid	3.82(7)	56.3	4.225	64.6
Br3···Centroid	4.35(4)	61.2	4.355	60.0
Br4···Centroid	4.15(5)	52.8	4.661	45.9
[FeBr]⁻···[Dimim]⁺ (potential π−d interactions)				
Fe···Centroid	4.45(2)	84.3[c]	4.475	80.8
Br2···C2	3.95(8)		3.815	
Br1···N1	3.88(5)		4.523	
Br4···C4	4.24(7)		3.815	
Br1···Centroid	4.26(5)	51.9	4.080	65.3
Br2···Centroid	4.54(7)	50.2	4.225	56.1
Br3···Centroid	4.59(5)	82.3	6.898	82.1
Br4···Centroid	6.91(6)	60.0	4.581	50.8

[a]Hydrogen bond not allowed according to IUPAC considerations (angle > 110°). [b]Long distance to be considered a relevant hydrogen bond. [c]Angle between Fe−Centroid vector and the imidazolium ring plane. [d]Distance from Br4 to the center of the N1−C2 bond.

In the unit cell, there are three different Br···Br interaction distances smaller than the sum of the vdw radii (<3.9 Å) between $[FeBr_4]^-$ tetrahedra, propagating them in a zigzag manner along the *b* axis [3.69(7) Å] and as linear chains along the *a* and *c* directions [3.71(7) and 3.83(5) Å, respectively]. The 2_1 screw axis changes the relative orientation of both the metal complex anions and the molecular cations from layer to layer (see Figure 1), passing through the center of the imidazolium ring and causing the antiparallel stacking of the $[Dimim]^+$ cation along the *b* direction. The $[FeBr_4]^-$ units have a slightly distorted tetrahedral geometry with a mean Br−Fe−Br bond angle of 107(6)° and a mean Fe−Br bond distance of 2.43(4) Å. All the refined values for the C−C and C−N bond lengths lie in the expected range of other imidazolium compounds, as for example in Bmim$_2$[XCl_4] (X = Fe, Ni, and Co)[34] and Emim[$FeCl_4$].[27a] Inside hybrid organic−inorganic materials, like the present compound, an anion could interact with a cation π system through three different modes: (i) hydrogen bonding, (ii) strong noncovalent anion−π interactions, where the anion will reside above the center of the aromatic ring, (iii) weak noncovalent anion−π interactions, where the anion will be located outside the periphery of the π system.[35] Taking the crystallographic data and comparing these with each specification rule of these interactions, Dimim[$FeBr_4$] could form: hydrogen bonds and weak anion−π interactions between $[FeBr_4]^-$ and $[Dimim]^+$ (Figures 2 and 3). On one hand, there are six hydrogen bonds according to the IUPAC rule[36] [Br···H interaction distances smaller than the sum of the vdw radii (<3.15 Å) and C−H···Br angle > 110°], the shortest one involving the H4 atom of the imidazolium ring[37] (Figure 2 and Table 1). Surprisingly, the most acidic hydrogen of the ring (H2) is at 3.20(5) Å to the closest Br atom, this distance being too long to consider its participation in the hydrogen-bond network as relevant. This issue differs from the data reported for the Emim$_2$[MCl_4] (M = Co, Ni, and Fe)[34] and Dimim[Cl] ionic liquids,[38] where the shortest hydrogen bond distance was located in this position. However, a similar behavior was observed in the Emim[BF_4],[39] Emim[$FeCl_4$],[27a] and Dimim-[$FeCl_4$][29] ionic liquids. On the other hand, for anion−π interactions, the nearest imidazolium centroid···Br^- distances vary from 3.82(1) to 4.26(1) Å (Figure 3a and Table 1). The

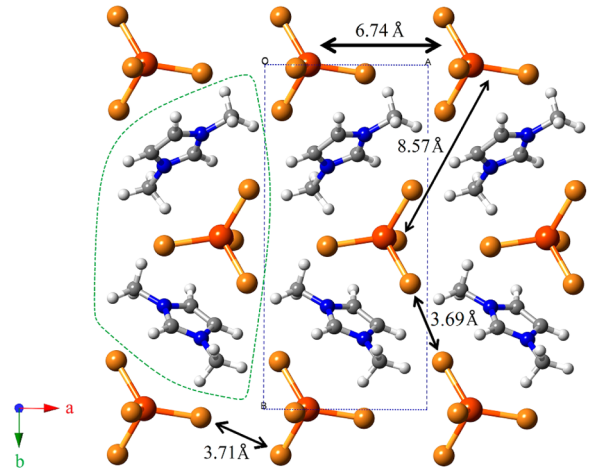

Figure 1. Crystal packing in the *ab* plane of Dimim[$FeBr_4$] crystal structure at 300 K. Orange (iron), gold (bromine), gray (carbon), blue (nitrogen), and white (hydrogen). The blue and green dashed squares represent the unit cell and the part of the crystal structure, which is plotted in Figure 3, respectively.

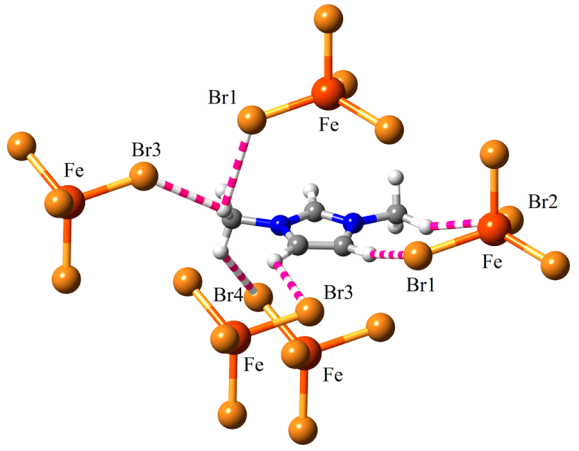

Figure 2. Hydrogen-bonding network in Dimim[$FeBr_4$] (H−Br contact up to 3.10 Å are marked with pink and white stripes).

dx.doi.org/10.1021/ic500882z | Inorg. Chem. 2014, 53, 8384−8396

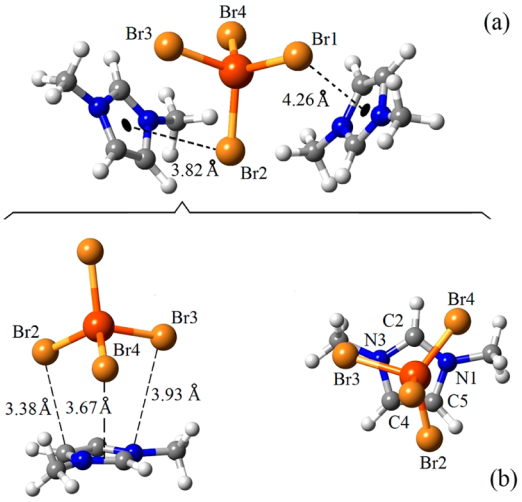

Figure 3. Potential π−d interactions between the metal complex and (a) imidazolium centroid and (b) imidazolium periphery (two views). Relevant distances and orientations are shown for the strongest interactions.

angles of the Br···centroid axis to the plane of the imidazolium rings range between 56(1) and 52(1)°. These distances and angles are in disagreement with the rule for strong Br−π interactions, where the bonding contact should be shorter than the sum of the vdw (≤3.75 Å) and the bromine should be located over the center of the π system (θ = 90 ± 10°).[35] It should also be mentioned that in the case of other organic−inorganic systems with anion−π interactions involving the $[MX_n]^{m-}$ metal complex, instead of the anion−π interaction residing above the ring centroid, it is usually located above the ring periphery,[40] this being characteristic of weak anion−π interactions. Indeed, Dimim[$FeBr_4$], which presents two contacts smaller than the sum of the vdw radii of Br···C and Br···[C−N] (≤3.75 and 3.70 Å, respectively) [Br2···C5 and Br4···[N1−C2] distances of 3.38(5) and 3.67(5) Å, respectively], could present some electrostatic interactions between the metal complex anions and the electron-deficient imidazolium rings. These experimental results, which will confirm the favorable nature of weak anion−π interactions between imidazolium and tetrabromideferrate ions, will be further analyzed below in the theoretical part.

3.2. Physical Characterization. *3.2.1. Spectroscopy Measurements.* Together with the crystal structure, Mossbauer, Raman, and far-IR spectroscopies offer the most rewarding means for studying the bonding and type of ionic liquid anionic species.[41] In particular, Raman spectroscopy provides the most useful, versatile, and straightforward technique for the study of metal coordination environments of MILs. Moreover, the Mossbauer effect allows a quantitative measurement of the covalent degree of the chemical bonding. This information derives from the Mössbauer isomer shift, which depends on the s-electron density at the Fe nucleus.

Figure 4a shows the nonpolarized Raman spectrum of the Dimim[$FeBr_4$] sample between 50 and 400 cm^{-1} at 300 K with 647 nm excitation. The $[FeBr_4]^-$ iron complex belongs to the symmetry point group T_d and has four Raman-active vibration modes; two of them are attributed to the bending modes [ν_s = 70 and ν_{as} = 89 cm^{-1}], while the others are related to the stretching modes [ν_s = 201 and ν_{as} = 222 cm^{-1}] of the Fe−Br bond. Moreover, in the presented frequency region, two modes

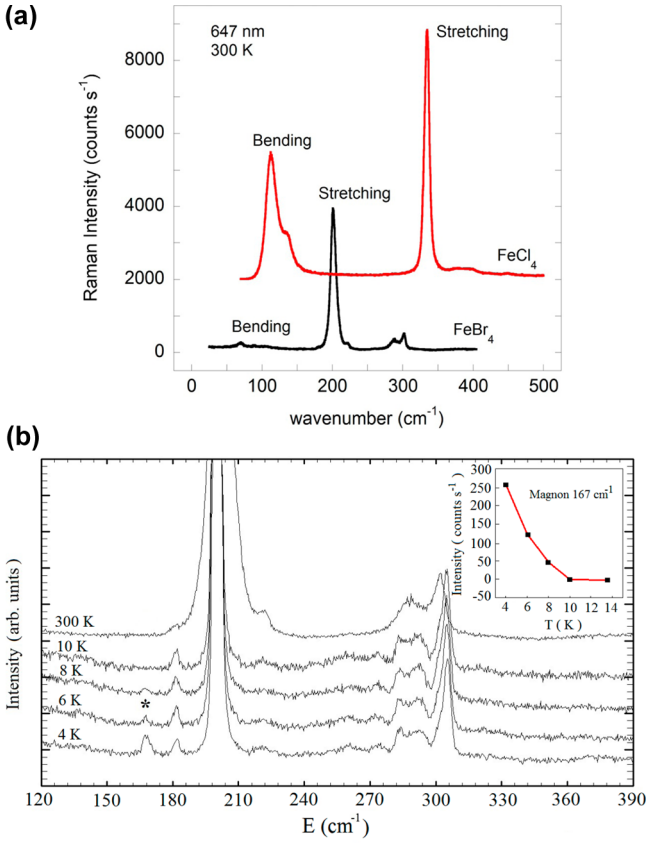

Figure 4. (a) Raman spectra of Dimim[$FeBr_4$] and Dimim[$FeCl_4$] between 30 and 500 cm^{-1} at 300 K. (b) Raman spectra of Dimim[$FeBr_4$] between 120 and 390 cm^{-1} at 300 K and from 4 to 10 K. (inset) The temperature dependence of the intensity of the magnon scattering, marked with * symbol in the picture. The red line is only a visual guide.

at 288 and 302 cm^{-1} are also detected, which correspond to the bending vibrations of CH_3−N and CH_2−N bonds of imidazolium cation, respectively.[42]

An estimation of the vibration bending and stretching modes of the $[FeBr_4]^-$ metal complex can be performed starting from the position of the $[FeCl_4]^-$ Raman bands, which has been broadly studied in the literature. In this case, the reported spectrum has been compared with the Dimim[$FeCl_4$] sample[29] (see Figure 4), taken under the same experimental conditions. The Raman frequency can be described approximately by formula 1

$$\nu = \frac{1}{2\pi}\sqrt{\frac{\kappa}{\mu}} \quad (1)$$

where κ and μ are the bond strength and the reduced mass, respectively. Considering the difference between the atomic weight of Cl and Br, the Raman frequencies of the $[FeBr_4]^-$ metal complex can be scaled as $\nu FeBr_4 = \nu FeCl_4/1.55$, assuming constant bond strengths. Thus, the estimated values obtained are [ν_s = 73 and ν_{as} = 88 cm^{-1}] and [ν_s = 215 and ν_{as} = 243 cm^{-1}] for the bending and stretching modes, respectively, showing a good agreement with the experimental ones. Finally, we have also compared the Raman spectrum of Dimim[$FeBr_4$] with another hybrid organic−inorganic material based on the $[FeBr_4]^-$ ion, namely, tetrabutylammonium tetrabromoferrate, TBA[$FeBr_4$] (see Figure S.3 of Supporting Information). As can be seen, the frequencies of the iron

dx.doi.org/10.1021/ic500882z | Inorg. Chem. 2014, 53, 8384−8396

complex appear almost at the same position, confirming that the assigned bands are related with the dominant iron-containing species $[FeBr_4]^-$.[43,44]

The Mössbauer spectra of Dimim$[FeBr_4]$ at 78 and 10 K (see Figure S.4 of Supporting Information) consist of a quadrupole doublet with a quadrupole splitting (QS) smaller than the line widths. This result is in good agreement with Raman spectroscopy and the reported data of an analogous tetrahalometallate ionic liquid, choline$[FeCl_4]$,[45] indicating a small electric field gradient at the iron nucleus. This small electric field gradient evidence a highly symmetric electric charge distribution about the iron metal complex with the sp^3 orbitals giving rise to an almost perfect tetrahedral environment. The estimated isomer shift (IS) (relative to metallic Fe at 295 K) of Dimim$[FeBr_4]$ in the paramagnetic state (10 K) displays a value of 0.37 mm/s, which is higher than those observed for choline$[FeCl_4]$ (see Table S.4 of Supporting Information). The increase in the positive isomer shift in the tetrahaloferrates as the number of bromides in the coordination sphere increases indicates a decrease in the s-electron density at the iron nucleus, which is just the opposite from what one would predict based upon covalency considerations. The Fe−Br bond is more covalent than the Fe−C1 bond, and thus one would expect the s-electron density at the Fe nuclei in $[FeCl_4]^-$ to be lower than that for $[FeBr_4]^-$, causing a higher IS in $[FeCl_4]^-$. The actual lower s-electron density at the iron nucleus in $[FeBr_4]^-$ as compared to $[FeCl_4]^-$ can be accounted for if the nonbonding interactions in these complexes is considered in addition to the iron-halide σ bond formation.[46] The ability to form π bonds between p electrons of the halides with partially filled t_2 orbitals of Fe^{3+} as well as halogen−halogen and anion−π interactions is stronger in the bromide than it is in the chloride derivatives. This leads to a higher 3d electron density in $[FeBr_4]^-$. The increased screening effect on the 4s electrons accounts for the reduction in the s electron density at the iron nucleus in $[FeBr_4]^-$ relative to that of $[FeCl_4]^-$, producing a higher IS. These results will be confirmed below with the calculation of the spin density distribution in the metal complex anion by DFT studies.

The low-temperature dependence (4−10 K) of the Raman modes of Dimim$[FeBr_4]$ in the spectral region of 120−390 cm^{-1} is shown in Figure 4b. First, no splitting of the stretching modes of the $[FeBr_4]^-$ metal complex appears when the temperature decreases (see spectra of 300 and 4 K), which is associated with no solid−solid phase transition,[29] in good agreement with crystallographic studies. Second, a shifting and narrowing of Raman bands are observed, which is attributed to temperature effect. Third, when the sample was cooled below T_N (see spectra below of 8 K), the spectra display a new weak broad Raman band, visible near 169 cm^{-1}, which becomes sharper as the temperature is further decreased. This new Raman band is mostly consistent with magnon scattering, whose integrated intensity in function of temperature is presented in the inset of Figure 4b. On the basis of their relatively high frequency, it is unlikely that the magnetic-order-induced bands correspond to one-magnon excitations, that is, single spin-flip processes with wave vectors at the center of the Brillouin zone. In comparative terms, the magnon excitation frequencies appear in rare-earth ortho-ferrites, such as $RFeO_3$ (R = Dy, Ho, Er, and Sm), below 25 cm^{-1}.[47] So, it would be more realistic to analyze the magnetic excitations under the assumption that they involve two-magnon processes, such as in the well-known cases of manganites[48] or cuprates.[49]

To the best of our knowledge, there are no model calculations of Raman-active magnetic excitations in the antiferromagnetic structures of hybrid organic−inorganic materials that could resemble Dimim$[FeBr_4]$. Therefore, at this stage we can analyze only qualitatively the magnetic excitations in this material. Finally, when the temperature decreases below 10 K, another well-defined Raman mode is observed at 180 cm^{-1}, which was masked by the broadening of the symmetric stretching mode of ν_s = 201 cm^{-1} at room temperature. At this moment, we do not have an assignment of this new Raman band unless the small distortion of the tetrahedron $[FeBr_4]^-$, due to temperature effect, could produce a splitting of the symmetric stretching mode.

3.2.2. Magnetization Measurements. Figure 5 shows the temperature dependence of the molar magnetic susceptibility

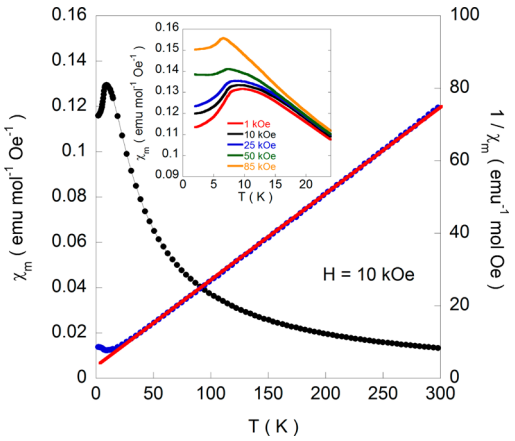

Figure 5. Temperature dependence of χ_m and $1/\chi_m$ for Dimim$[FeBr_4]$ measured under 1 kOe. The solid red line is the fit according to eq 2 of the manuscript. (inset) The low-temperature ZFC magnetic susceptibility at different fields from 1 to 85 kOe. The curves were shifted 0.01 emu/mol Oe for clarity.

(χ_m) and inverse susceptibility ($1/\chi_m$) curves of Dimim$[FeBr_4]$, measured at 1 kOe after cooling without an applied magnetic field (zero-field cooling (ZFC)). As can be seen, the molar magnetic susceptibilities increase with decreasing temperature to 9.2 K, where a broad maximum (with an inflection point located at 7.60 K) is observed, indicating that a long magnetic order is established (see inset of Figure 5). The magnetic data were fitted in the paramagnetic range using the Curie−Weiss law for $S = 5/2$ in the molecular field approximation,[50] eq 2, to clarify the significance of magnetic exchange between the Fe^{3+} ions in the crystal lattice

$$\chi_m = \frac{C}{T - \theta_p} = \frac{N\mu_0\mu_B{}^2 g^2 S(S+1)}{3k_B\left(T - \frac{zJS(S+1)}{3k_B}\right)} \quad (2)$$

where N is Avogadro's number, g is the spectroscopic splitting factor, μ_B is the Bohr magneton, k_B is the Boltzmann constant, J is the exchange coupling parameter defined by $H_{ex} = \sum_{nn} 2JS_i \cdot S_j$, and z is the number of nearest neighboring Fe^{3+} atoms. The least-squares fit of the experimental data from 20 to 300 K (see Figure 5), with $z = 4$, gives a J value of −1.28 K. This small value points to weak antiferromagnetic interactions, in accordance with the large distances between the iron-complex anions and the literature values for this type of magnetic pathway.[51] The Curie constant (C) and Curie−Weiss temper-

dx.doi.org/10.1021/ic500882z | Inorg. Chem. 2014, 53, 8384−8396

ature (θ_P), obtained by the fitting, have values of 4.25 emu K/mol Oe and −14.9 K, respectively. This Curie constant corresponds to an effective paramagnetic moment μ_{eff} = 5.75 μ_B/Fe ion, in good agreement with the expected value of 4.38 emu K/mol Oe (5.92 μ_B) for Fe^{3+} ion with a magnetic spin S = 5/2.[52] Moreover, to study the magnetic field dependence of the 3D magnetic ordering with the applied magnetic field, another set of DC magnetic susceptibility measurements were performed from 1 to 85 kOe and between 2 and 25 K, after cooling in absence of the applied field (see inset of Figure 5). Switching to higher fields, the inflection point of χ_m observed at 7.60 K under 1 kOe field moves weakly to lower temperatures, being located at 6.80 and 6.60 K for an applied field of 25 and 85 kOe, respectively.

The field dependence of the magnetization at 15 K shows a lineal behavior in the whole applied field range confirming the paramagnetic behavior at this temperature (see Figure 6). At 2

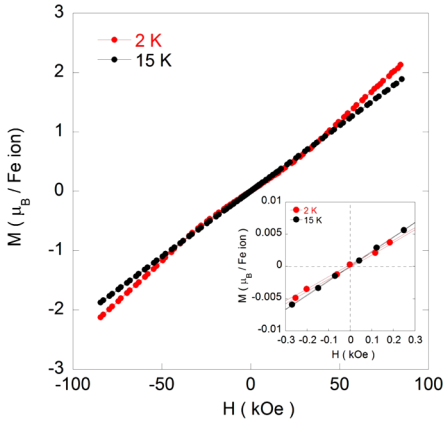

Figure 6. Magnetization vs applied magnetic field at 2 and 15 K for Dimim[$FeBr_4$]. (inset) An enlargement of the low-field region.

K, in the ordered state, the magnetization shows no hysteresis, thereby discarding the existence of any ferromagnetic component. Moreover, it continuously increases, without showing any tendency to saturation, to 85 kOe. The value obtained in this magnetic field (2.15 μ_B/Fe ion) is far from the expected fully saturated value for a Fe^{3+} ion (5 μ_B/Fe ion), confirming the presence of a noticeable magnetocrystalline anisotropy within the material. This issue differs from the data reported in other MILs based on tetrachloroferrate exhibiting 3D ordering, where the magnetization tends toward saturation for magnetic fields larger than 60 kOe.[27a,53,29] Finally the magnetization presents an inflection point near 35 kOe, which may suggest a metamagnetic behavior; therefore, this could be the result of a canted magnetic structure that becomes progressively collinear under the effect of the magnetic field (see below the description of the magnetic structure).

To study a possible dynamical response due to magnetic ordering, AC magnetic susceptibility measurements were performed with an alternate excitation field (H_{ac}) of amplitude 10 Oe and frequencies from 100 to 10 000 Hz (see Supporting Information, Figure S.5). The curves display a broad peak in the real component of the susceptibility χ' near 9 K, confirming the existence of long-range order interactions. The weak absorption in the imaginary component χ'' in this temperature range ratifies the presence of an antiferromagnetic order, in good agreement with the results obtained above from the molar magnetic susceptibility data; moreover, it excludes the existence of a possible dynamical magnetic process at low temperatures.[54]

3.2.3. Heat Capacity Measurements. The temperature dependence of the molar heat capacity (C_P) for Dimim[$FeBr_4$] is presented in Figure 7. Calorimetric measurements in the

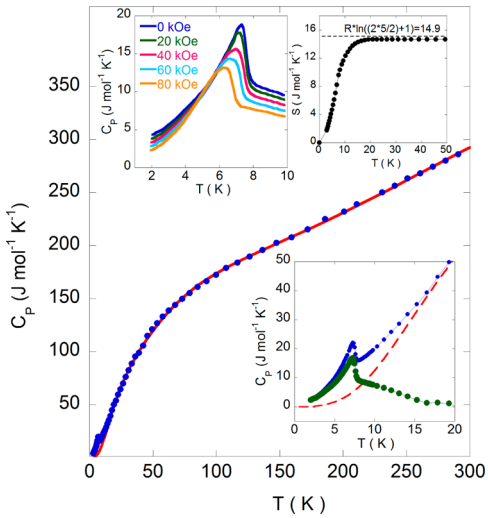

Figure 7. Specific heat of Dimim[$FeBr_4$] between 2 and 300 K. Experimental data (blue full dots), estimated phonon contribution (red line), and magnetic contribution (green dots). (lower inset) The magnetic contribution at low temperatures. (upper-right inset) The magnetic entropy variation as a function of temperature. (upper-left inset) The magnetic specific heat as a function of temperature in the presence of external magnetic fields ($0 \le H \le 80$ kOe).

absence of external magnetic field reveal a maximum (ΔC_P = 4.9 J/molK) centered at 7.3 K (see lower inset in Figure 7). This anomaly displays the typical λ shape appearance of a second-order transition, which can be related to the establishment of a 3D antiferromagnetic order, in good agreement with the magnetic susceptibility data. Above T_N = 7.7 K, defined as the inflection point of the maximum, C_P increases continuously as a result of the phonon contribution and does not show any tendency to saturation even up to room temperature, where the value of C_P is 290.3 J/mol K, still far from the expected value (525 J/mol K) according to the Dulong and Petit law.[55] This behavior is attributable to the presence of a high number of hydrogen atoms within the imidazolium cation, which display very high excitation energies.[56]

To extract the magnetic contribution (C_{mag}), the phonon contribution (C_{pho}) should be determined. The exact calculation of C_{pho} is difficult due to the absence of a suitable nonmagnetic isomorphous ionic liquid. Thus, an estimation of C_{pho} was obtained using the Debye model[57] and considering the existence of three Debye temperatures, the smaller one (θ_1) related to the heavy ions, such as Fe and Br (n_1), (θ_2) linked to the C and N ions (n_2), and the higher one (θ_3) associated with the H light ions. The best fit to the experimental data from 15 to 300 K is obtained for θ_1 = 86 K, θ_2 = 293 K, θ_3 = 1720 K, n_1 = 4.22, n_2 = 4.00, and n_3 = 12.78 ions. The temperature dependence of the magnetic contribution (C_{mag}) is shown in the lower inset of Figure 7. The jump of C_{mag} at T_N, ΔC_{mag} = 14.7 J K^{-1} mol^{-1} is 25% smaller than the expected one for an antiferromagnetic structure with S = 5/2, ΔC_{mag} = 19.6 J K^{-1} mol^{-1}, within the molecular field approximation.[58] This feature could be attributed to the presence of spin fluctuations. Apart

dx.doi.org/10.1021/ic500882z | Inorg. Chem. 2014, 53, 8384−8396

from the maximum associated with the 3D magnetic order around 7.3 K, another anomaly like a shoulder from 8 to 15 K is observed. One of the most plausible explanations for this magnetic anomaly is the contribution to the magnetic heat capacity of the Fe−Br···Br−Fe magnetic couplings in the form of two-dimensional (2D) ordering.[59] This would be located inside the layers, as ferromagnetic coupling, as will be discussed later from magnetic structure data. The magnetic entropy variation calculated as $\Delta S = \int (Cm/T)dT$ is shown in the right-upper inset of Figure 7. As can be seen, it becomes gradually larger with increasing temperature, reaching at about 20 K a value very close to 1.79 R = 14.9 J mol^{-1} K^{-1}, which corresponds to the full entropy coming from the magnetic specific heat based on the degenerate freedom of S = 5/2. By applying magnetic fields (see left-upper inset of Figure 7), the inflection point of the λ peak shifts to lower temperatures, displaying a T_N = 7.60 and 6.90 K at 40 and 80 kOe, respectively, which almost correspond to those obtained from the magnetic susceptibility data. These results confirm that the magnetic order is antiferromagnetic and that the spin of the trivalent iron ions (Fe^{3+}) is a high-spin state (S = 5/2). In addition, the magnetic peak does not disappear for fields larger than 80 kOe, corroborating the presence of the magneto-crystalline anisotropy detected in the magnetic susceptibility data.

3.3. Description of the Magnetic Structure. The temperature evolution of the D1B patterns between 2 and 10 K (see Figure 8) shows the appearance of additional elastic

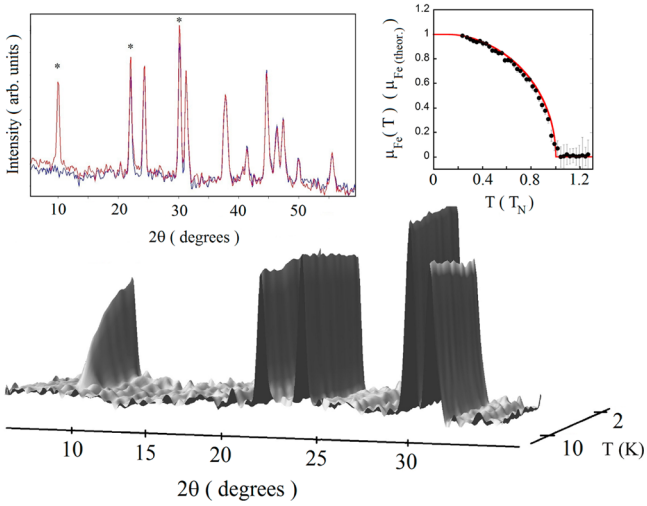

Figure 8. Neutron thermodiffractogram collected at D1B diffractometer between 2 and 10 K. (left inset) The neutron diffraction profiles of Dimim[$FeBr_4$] at 10 (blue) and 2 K (red) obtained in D1B. The (*) dots show the magnetic contributions. (right inset) The temperature dependence of the normalized Fe magnetic moment (calculated from μFe(T)/μFe, the μFe being the theoretical value of ca. 5 μ_B) obtained from the fit of the neutron diffraction pattern and the expected theoretical dependence for the Brillouin function with S = 5/2 (red line).

intensity at temperatures below around 8 K, confirming the onset of a magnetic ordering (T_N = 7.6 K). A comparative view of the nuclear pattern (10 K) as different from the magnetic ones (2 K) reveals the occurrence of a long-range magnetic ordering due to the presence of an extra magnetic signal in some structural reflections [see left inset of Figure 8], compatible with the magnetometry results. Moreover, a weak diffuse scattering superposed to the 3D ordering is detected below around 2θ = 15°, which increases in a monotonous way below T_N (not shown), suggesting a complex magnetic transition.[60] A structural phase transition was discarded as the origin of this diffuse scattering. Rietveld refinements above the magnetic phase transition show that the $P2_1$ symmetry of the crystal structure is maintained down to 2 K; only a slight shift of the Bragg reflections associated with lattice contraction was observed. Therefore, further studies are required to understand the origin of this diffuse scattering, which also was detected in Dimim[$FeCl_4$].[29]

Focusing on the long-range magnetic ordering, below T_N, the additional elastic intensities can be indexed with the propagation vector $\mathbf{k}$ = (0, 0, 0), indicating that the magnetic and nuclear unit cells are the same.

To determine the possible magnetic structures, the irreducible representations (irreps) compatible with the indexed propagation vector [$\mathbf{k}$ = (0, 0, 0)] were investigated using Bertaut's symmetry analysis method.[61] This approach allows us to determine the symmetry constraints between the different magnetic moments of the Fe^{3+} atom within the magnetic unit cell. The total magnetic representation of the propagation vector group can be decomposed on two irreducible representations, each one of three dimensions with three basis vectors, and therefore the G_{mag} can be represented as

$$G_{mag} = 3(G_1 + G_2)$$

leading to two possible spin configurations:

$$G_1: A_X = S_1^x - S_2^x,\ F_Y = S_1^y + S_2^y,\ A_Z = S_1^z - S_2^z$$

$$G_2: F_X = S_1^x + S_2^x,\ A_Y = S_1^y - S_2^y,\ F_Z = S_1^z + S_2^z$$

where S_i^x is the component along x of the magnetic moment of atom (i). Note that there are two Fe^{3+} ions in the magnetic unit cell that are symmetry-related (Wyckoff position 2a). The magnetic moments for Fe(2a) atoms on each sublattice are obtained from the basis vectors as $\mathbf{m}_{2a}(1) = (u, v, w)$ and $\mathbf{m}_{2a}(2) = (-u, v, -w)$ for irrep G_1 and $\mathbf{m}_{2a}(1) = (u, v, w)$ and $\mathbf{m}_{2a}(2) = (u, -v, w)$ for irrep G_2. In both cases there are three degrees of freedom (u, v, w) for the magnetic structure.

The magnetic model described by irrep G_1 corresponds to ferromagnetic layers, which are antiferromagnetically coupled along the b axis with a canting that could produce a global ferromagnetic behavior, extended into the ac plane. The magnetic structure described by irrep G_2 can be seen as antiferromagnetic chains running along the b axis with a canting into the ac plane. Rietveld refinement of the 2 K pattern, where the atomic coordinates and isotropic temperature factors of the nuclear part were fixed to those obtained from the High-Resolution Powder Diffractometer for Thermal Neutrons (HRPT) and DFT calculations, respectively, shows that G_1 is the only irrep that provides a satisfactory agreement between the calculated and the experimental diffraction patterns. Therefore, using G_1 we are able to obtain the relative orientation of the magnetic moments of the two symmetry-related magnetic sites present in this MIL. The Shubnikov group corresponding to G_1 is $P2_1$, and therefore the space group remains invariable after the magnetic phase transition. To avoid overparameterization and due to the negligible value obtained in the first refinements for the magnetic moment component along the b axis, it was fixed at zero, giving rise to a collinear antiferromagnetic behavior, with the magnetic mo-

dx.doi.org/10.1021/ic500882z | Inorg. Chem. 2014, 53, 8384−8396

ments parallel to the *a* axis (refinement of the *c* axis was also 0), which is in good agreement with the macroscopic magnetic measurements. The final refinement is shown in Figure S.6 of Supporting Information, and the corresponding magnetic structure is shown in Figure 9. The nuclear and magnetic discrepancy factors are R_p = 22.0, R_{wp} = 14.4, R_{Bragg} = 8.37, and R_{mag} = 5.24.

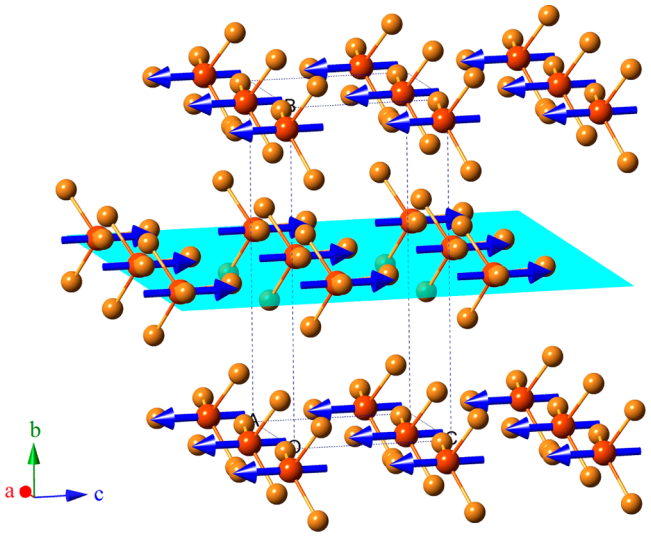

Figure 9. Magnetic structure of Dimim[$FeBr_4$]. The magnetic moments of Fe^{3+} are in the *c* direction. The dashed lines represent the unit cell.

Out of all the possible orientations, the collinear solution proposed by G_1 gives the best agreement between observed and calculated patterns. The magnetic moment obtained is the one refined to 4.75(6) μ_B, slightly lower than the expected value of 5 μ_B for Fe^{3+} in high-spin configuration, which could be attributed to the diffuse magnetic background observed below T_N. In addition, the possible metamagnetic transition observed at 35 kOe (see inset of Figure 6) could be interpreted based on the hypothesis that the magnetic structure proposed would not be "strictly" collinear, showing a small canting in the *b* axis, which has not been detected by neutron powder diffraction. Finally, sequential refinements against these data were performed using the FullProf suite[61b] to follow the evolution of the magnitude of the magnetic moment with the temperature. The temperature dependence of the modulus of the Fe magnetic moment, μ_{Fe}, obtained from the refinement between 2 and 10 K is given in the right inset of Figure 8, compared with the theoretical dependence corresponding to the Brillouin type $S = 5/2$.[62]

3.4. Density Functional Theory Calculations. A parallel theoretical study for the crystal and magnetic structure of Dimim[$FeBr_4$] was carried out by DFT calculations as implemented within the SIESTA[30] code. As already explained in Section 3.1, we carried out a structural relaxation to refine the atomic coordinates starting from an approximation of the experimental coordinates after the first Rietveld analysis. In addition, we assumed the antiferromagnetic A phase (G_1) obtained by neutron diffraction studies, as discussed in Section 3.3. The intramolecular geometries (reduced coordinates) and distances of the $[Dimim]^+$ cation and $[FeBr_4]^-$ anion obtained by DFT are not too far away from the starting point, with only an overestimation of about 3% from the experimental data, within the standard deviations of the functional approach.[32]

Previous theoretical studies have shown that an electron-donor molecule (anion) can experience favorable binding interactions with the π cloud of an electron-deficient aromatic ring, such as in pyridine[63] or azines[64] derivatives. However, the anion$-\pi$ interactions with imidazolium π systems are extremely rare and only recently studied in calix[*n*]imidazolium,[65] hydrogen bonding being the predominant interaction motif. According to the structural studies, Dimim[$FeBr_4$] exhibits remarkable features that would support the existence of attractive anion$-\pi$ interactions[66] between the tetrabromoferrate anion and the dimethylimidazolium cation, this being, to our knowledge, the first evidence of an MIL.

The binding energy between a metal complex and an aromatic ring depends on the halide of the $[MX_n]^{m-}$ anion, the geometric features (lineal, trigonal planar, square planar, tetrahedral, or octahedral), and the different orientations adopted by the metal complex.[22] To confirm the existence of the anion$-\pi$ interactions in Dimim[$FeBr_4$] we have pursued two different pathways. The first is to compute the "ionization energy" of the gas phase, defined following ref 32 as $E_I = E_{pair} - (E_{cat} + E_{an})$, where E_{an} and E_{cat} are the energies of the $[FeBr_4]^-$ and the $[Dimim]^+$ ions, respectively, and E_{pair} is the ion-pair ground state energy. All the calculations for the isolated Dimim[$FeBr_4$] and the corresponding charged constituents were performed in cubic supercells of 25 Å per side, with a compensating uniform background of the opposite charge to avoid the divergence of the electrostatic potential in charged periodic systems. The same correction energy for the isolated ions as in ref 32, proposed initially by Leslie and Gillan[67] and also for G. Makov and M. Payne,[68] was used here. The ionization energy amounts to −3.17 eV/pair. Thus, these simulations show that the anion$-\pi$ interactions are energetically favorable at least in the gas phase.

To further check their existence in the condensed phase, we studied as a second step the projected density of states (PDOS) of the imidazolium with the bromines of the $[FeBr_4]^-$ metal complex, depicted in Figure 10a. We observed a wide range of energies between 1 and 3 eV below the Fermi energy, where the PDOS on the imidazolium and on the metal complexes take a nonzero value, proving the existence of a chemical bonding between them. To visualize the shape of one of these states that can be described by a linear combination of the atomic orbitals of the $[Dimim]^+$ and the $[FeBr_4]^-$ complex, we chose a representative state at the Γ point, with an energy of 1.65 eV below the Fermi energy, corresponding to the position where the PDOS show the peak marked in Figure 10a. The isosurface for a value of the wave function of 0.02 is shown in Figure 10b and shows how the wave function can connect two $[FeBr_4]^-$ anions from layer to layer across the π orbital of the imidazolium ring. Thus, an electronic transmitting mechanism can be propagated via anion$-\pi$ interactions. Interestingly, the wave function is located above the ring periphery, rather than residing above the ring centroid, which is characteristic of weak anion$-\pi$ interactions; this is in good agreement with crystallographic studies.

For the study of the possible magnetic superexchange pathways in MILs, it is important to know the spin density distribution in the metal complex anion. As happened with Dimim[$FeCl_4$],[29] in the present compound, there is a partial transfer of charge from the iron atoms to the bromine atoms due to the partial covalent bond. This issue strengthens the

dx.doi.org/10.1021/ic500882z | Inorg. Chem. 2014, 53, 8384−8396

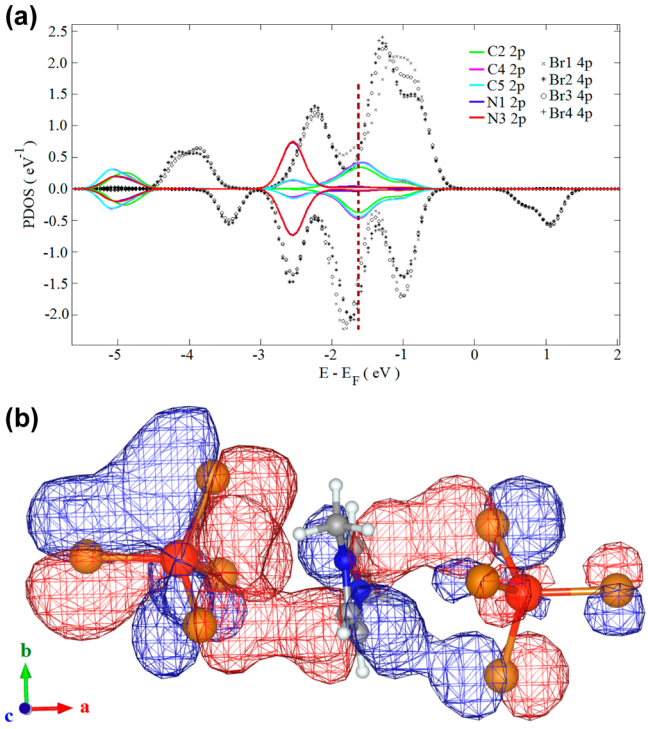

Figure 10. (a) PDOS of bromines from a $[FeBr_4]^-$ ion (black marks) with the atoms in the imidazolium ring (color lines). Dashed line shows the state with energy of −1.65 eV below the Fermi energy, where there is orbital overlapping. (b) Representation of the wave function for this state (red and blue colors represent the positive and negative part, respectively).

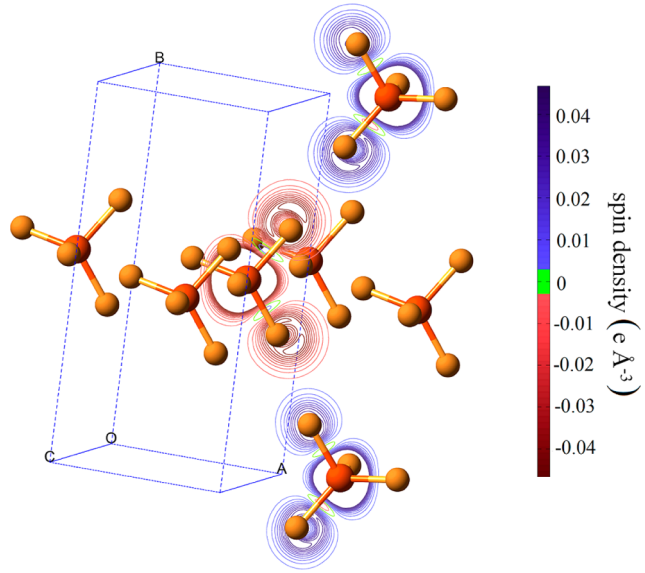

Figure 11. Schematic view of the projection of the induced spin density for the interplane exchange magnetic interaction, through Fe−Br−Br−Fe bridges, at 0 K. The levels are 0.05 e Å^3 with steps of 0.005 e Å^3. Only the low-density levels are drawn. Blue and red colors represent the opposite sign of the spin density.

interaction between two iron atoms through superexchange pathways, type Fe−Br···Br−Fe. To further check the stability of the antiferromagnetic A phase, with spin configuration type G_1 (see Section 3.3), we compared the difference in energy with respect to the ferromagnetic one, type G_2. The data display lower energy [−5.38 (ev/cell)] for the G_1, in good agreement with the result obtained by the experimental data. Figure 11 shows the spin delocalization for the most stable magnetic structure (type A), integrated in the plane containing two irons and two bromines. The different sign in the spin density along the *b* direction is related to the antiferromagnetic interaction between planes. Table S.5 of the Supporting Information shows the Mulliken charge obtained by DFT for the $[FeBr_4]^-$ anion. The sum of the Mulliken populations gives a value of 4.98 μ_B, which is expected for a Fe^{3+} with a high spin of $S = 5/2$. The quantity of spin transferred to the bromines ranges from 0.27 and 0.29 μ_B, the total transfer being 1.12 μ_B, which represents 22.4% of the magnetic moment. These numbers are consistent with a direct integration of the charge density over spheres surrounding atoms. Assuming nonoverlapping spheres around Fe and Br of 2.00 and 2.6 Bohr, respectively (whose sum equals the mean Fe−Br distance in the tetrahedra), the spin charge amounts to 3.6027 and 0.2262 μ_B. Finally, comparing the present result with those obtained for Dimim$[FeCl_4]$[29] (total spin density transfer from Fe to Cl = 1.05 μ_B, which symbolizes 21.0%), we find that the delocalization is slightly higher. This result is in good agreement with Mossbauer results and the reported data of other halometallate compounds with these types of superexchange pathways.[51b]

3.5. Magneto−Structural Correlations. The magneto−structural correlations of mixed organic−inorganic materials are attracting the interest of scientific community, with special attention toward the anion−anion and anion−donor−anion magnetic interactions.[69] In the case of the present MIL, the magnetic structure consists of an arrangement of iron metal complex groups, stabilizing the overall antiferromagnetic ordering (see Figure 9). If we consider their structural features, we can deduce that direct Fe···Fe interactions are not present. The shorter Fe···Fe distances through the space range between 6.74 and 8.57 Å (see Table 2), the superexchange interactions being responsible for the 3D magnetic ordering.

In the crystal structure of Dimim$[FeBr_4]$, all the $[FeBr_4]^-$ metal complexes are stacked upon one another in a 3D manner with three types of nonbonding interactions (a) hydrogen bond, (b) anion−π, and (c) bromine−bromine. Two of them can transmit magnetic couplings between an iron ion and its first shell of neighboring iron ions:[70] (i) direct superexchange anion−anion interactions (Fe−Br···Br−Fe) and (ii) indirect superexchange anion−anion interactions (Fe−Br···Im···Br−Fe), where Im represents an imidazolium donor cation. Figure 12 shows a scheme of the three possible magnetic interactions projected on the ac plane, according to the most appropriate model of the magnetic structure obtained from neutron diffraction data. The *J*1 interaction, $J\perp$ or interplane coupling, gives rise to zigzag chains to form a ladder structure that runs parallel to the *b* direction. It is supposed to be the strongest coupling, according to the predominant antiferromagnetic behavior of this material (see below the discussion of magnetic fitting calculations and Figure S.7 of Supporting Information). Furthermore, there are two intraplane interactions, defined by *J*2 or $J\|$, with similar (Fe−Br···Br−Fe) distances and angles, which connect the iron atoms in linear ferromagnetic chains in the ac plane. In both magnetic interactions, *J*1 and *J*2, the four ligand atoms involved in the magnetic pathways are bromines which are connected through a single superexchange pathway (Fe−Br···Br−Fe). In addition to these two interactions, two adjacent zigzag chains, coupled with Fe−Br···Br−Fe interactions in the *b* direction, can be connected via an imidazolium

dx.doi.org/10.1021/ic500882z | Inorg. Chem. 2014, 53, 8384−8396

Table 2. Selected Geometrical Parameters, Bond Lengths (Å) and Angles (deg) Obtained from High-Resolution Neutron Diffraction (Experimental at 10 K) and DFT (Calculated) Related to the Possible Magnetic Exchange Pathways for Dimim[$FeBr_4$]

magnetic exchange pathways	direct distance Fe–Fe, (Å)	length of exchange pathway, (Å)	bond, (Å) Fe–Br	bond, (Å) Br–Br	bond, (Å) Br–Fe	angle, (deg) Fe–Br–Br	angle, (deg) Br–Br–Fe	torsion angle τ, (deg)	direction
$J1$ (exp.)	8.57(2)	8.60	2.46	3.69	2.45	167.9	171.1	16.2	b
$J2$ (exp.)	6.74(4)	8.57	2.46	3.71	2.40	89.6	164.1	38.9	a
$J2$ (exp.)	6.76(3)	8.68	2.46	3.83	2.39	87.4	155.6	18.0	c
$J3$ (exp.)	8.75(1)	13.51	2.40	8.59	2.45	73.9	76.7		b
$J1$ (calc.)	8.945	8.959	2.426	4.108	2.425	175.0	172.6	17.1	b
$J2$ (calc.)	6.846	8.769	2.426	3.913	2.430	87.4	154.9	39.3	a
$J2$ (calc.)	6.851	8.872	2.425	4.031	2.416	83.6	156.3	19.2	c
$J3$ (calc.)	8.747	13.246	2.425	8.395	2.426	81.2	81.4		b

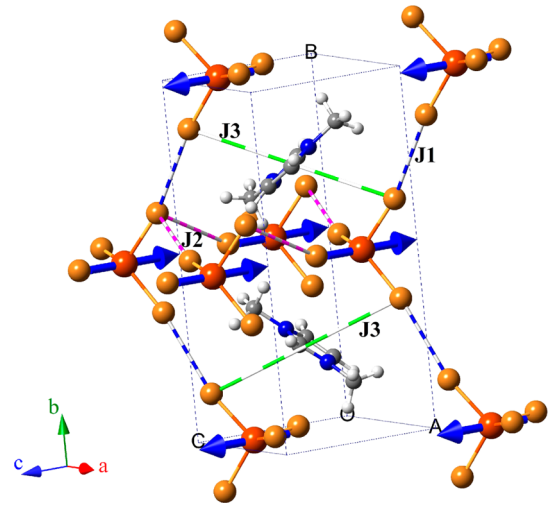

Figure 12. Schematic view of the possible magnetic exchange pathways for Dimim[$FeBr_4$] via Fe–Br···Br–Fe ($J1$ and $J2$) and Fe–Br···Im···Br–Fe ($J3$) bridges.

cation (Fe–Br···Im···Br–Fe). According to the magnetic structure obtained, these types of interactions will be antiferromagnetic, presenting direct Fe···Fe and Br···Im···Br experimental distances of 8.75 and 8.59 Å, respectively.

First, the strength of the magnetic exchange halide–halide nonbonding interactions between MX_4 metal complex (M = metal and X = halide) can be estimated according to these parameters: (i) X···X distance, (ii) M–X···X angles, and (iii) the M–X···X–M torsion angle (τ). In general, shorter X···X distances, larger M–X···X angles, and torsion angles near 0 and 180° are correlated with stronger magnetic exchange constants.[20] These parameters were estimated in the present MIL from the crystal structure obtained from neutron powder diffraction data [see Table 2 and the electronic Supporting Information (.CIF file)]. In relation to the Br···Br distances, the interplane ($J1$) and intraplane couplings ($J2$) range from 3.69 to 3.83 Å, this being smaller than the sum of the vdw radii of two bromine atoms (3.90 Å), which displays remarkable agreement with other reported magnetic coupling distances in several metal–organic materials.[71] For the second and third parameters, $J1$, which connects the tetrabromoferrate(III) anions in zigzag chains propagating along the b direction, presents a nearly lineal combination of Fe–Br···Br and Br···Br–Fe angles (167.9 and 171.1°) with τ = 16.2°. In the case of the intraplane interactions ($J2$), which give rise to linear chains in the ac plane, the magnetic couplings show a mixture of exchange angles: (i) Fe–Br···Br, which varies between 87.4 and 89.6° and (ii) Br···Br–Fe, which ranges from 155.6 to 164.1° with τ from 18.0 to 38.9°. Therefore, according to these considerations, the interplane magnetic interactions will be stronger than the intraplane ones due to their present shorter distances, larger angles, and a smaller torsion angle.

Second, the electrostatic effects and the deformation of electric charge around the halogen atom, in tetrahaloferrate(III) complexes containing the heteroaromatic organic cation, also play a crucial role in the force and type of nonbonding magnetic interactions.[72] These issues can be analyzed in the present MIL, with the results obtained from the DFT calculations. On one hand, the spin density delocalized onto the first four bromide neighborings is very uniform (ranging from 0.27 to 0.29). On the other hand, the electron density of

dx.doi.org/10.1021/ic500882z | Inorg. Chem. 2014, 53, 8384–8396

magnetic exchange interactions show a linear coupling (near to 180°) and out of-plane of angles for $J_{\perp}$ ($J1$) and $J\|$ ($J2$), respectively. Therefore, the orbital overlap between the two nonbonding bromide ions should be higher when the coupling is collinear. Thus, the interplane magnetic interactions should be stronger than intraplane ones, in good agreement with the overall antiferromagnetic behavior of this MIL.

Third, the quantitative analysis of the exchange couplings between the Fe^{3+} ions can be realized from the parameters experimentally obtained from magnetic measurements. On the basis of the previous estimations, we are able to consider the direct Fe−Br···Br−Fe superexchange coupling along the b axis, $J1$, as the main exchange pathway. In addition, on the ac plane, the orthogonal conformation of the Br−Br−Fe interactions promotes a weak orbital coupling, giving rise to a weak ferromagnetic coupling between Fe^{3+} ions. Another indirect exchange coupling is present in this complex, $J3$ (Fe−Br···Im···Br−Fe), which should be weakest, due to the involvement of an imidazolium ion (defined as $S = 1/2$)[73] inside the exchange pathway. On the basis of these considerations, the most appropriate model to treat the magnetic susceptibility data is a combination of a modified expression classical spin ladderlike chain (one-dimensional) together with a mean-field term to take into account the intraplane interactions (2D).[74] The model described by Fisher[75] [see eq 3] was carried out to extract the magnetic exchange couplings between the Fe^{3+} ions

$$\chi_{obs} = \frac{\chi_{1D}}{1 - \chi_{2D}} \tag{3}$$

defined as

$$\chi_{1D} = \frac{Ng^2{\mu_B}^2 S(S+1)}{k_B T} \cdot \frac{1+u}{1-u}$$

$$u = \coth(Y) - \frac{1}{Y};\ Y = \frac{JS(S+1)}{k_B T}$$

$$\chi_{2D} = \frac{2zj}{Ng^2{\mu_B}^2} \cdot \chi_{1D}$$

where J and j are the $J1$ and $J2$ magnetic interaction parameters and z is the number of nearest neighboring magnetic species ($z = 4$). The least-squares best-fit of the experimental data, from 2 to 300 K, gives the parameters $J = -2.38(1)$ K, $j = 0.017(1)$ K, and $g = 1.97(1)$. The calculated curve obtained (solid line in Figure S.7 of Supporting Information) reproduces quite well the magnetic data in the whole temperature range investigated, and the fitting parameters are in agreement with the hypothesis that the Fe−Br···Br−Fe interactions along the b axis are the strongest. Even when the quantitative analysis of the exchange couplings is not easy due to the occurrence of different exchange coupling, the proposed approach can be valuable in the absence of a more realistic model.

The comparison of the magneto−structural correlations of Dimim[$FeBr_4$] with the MIL analogue Dimim[$FeCl_4$][29] points to the fact that the larger antiferromagnetic ordering observed in the bromide compound [from Cl that shows the 3D magnetic ordering at 5.6 K to Br at 7.7 K)] cannot be attributed to the geometrical factor of nonbonding interactions. On one hand, the bigger the halide size is, the larger the distances between the iron−iron and superexchange magnetic pathways are. Therefore, a lower ordering temperature is expected in Dimim[$FeBr_4$]. On the other hand, both MILs display an almost linear coupling and out-of-plane magnetic exchange angles in $J1$ and $J2$, respectively. Thus, this enhancement of the antiferromagnetic interactions with the substitution of bromine for chlorine atoms can be attributed to the spin delocalization of iron atoms in the metal complex, which favors the magnetic couplings. Moreover, these issues can explain why the interplane magnetic coupling parameter $J1$, along the b axis, is higher in the case of the tetrabromide metal complex ($J1$ = −0.511[29] and −2.38 K for Cl and Br, respectively). Finally, the existence of weak ferromagnetic superexchange magnetic interaction in the ac plane ($J2$ = 0.017 K) is in contrast to the chloride drivative ($J2$ = −0.359 K; weak antiferromagnetic), and the presence of a new electrostatic mechanism across noncovalent interactions via an imidazolium cation (Fe−Br···Im···Br−Fe) opens up a new field of understanding and improving of the magneto−structural correlations within MILs.

CONCLUSIONS

A new 3D magnetic correlated ionic liquid based on imidazolium cation and tetrabromoferrate ions, namely, Dimim[$FeBr_4$], was synthesized and structurally characterized. This compound was obtained as a microcrystalline powder at room temperature and exhibits high thermal stability. The topological framework of its condensed phase is characterized by layers of cations $[Dimim]^+$ and anions $[FeBr_4]^-$, which change the orientation from layer to layer, stacked upon one another in a 3D manner with several nonbonding interactions: hydrogen bond, anion−π, and halide−halide. Magnetic studies show the existence of predominant antiferromagnetic interactions, exhibiting a 3D magnetic ordering below 8 K, together with the presence of magnetocrystalline anisotropy. The collinear antiferromagnetic structure is formed by ferromagnetic layers extended into the ac plane, which are antiferromagnetically coupled along the b axis. A spin delocalization reflects the fact that the magnetic molecular orbitals are spread over the bromine atoms, thus enhancing the magnetic interactions through a superexchange magnetic interaction mechanism, (Fe−Br···Br−Fe). In addition, the experimental and DFT calculations display that two $[FeBr_4]^-$ anions can connect across the π orbital of an imidazolium ring. These magnetic phenomena are responsible for the 3D ordering observed in the family of MILs based on the tetrahaloferrate ion and imidazolium cation, displaying a higher ordering temperature with a halide ion less electronegative in the metal complex.

ASSOCIATED CONTENT

Supporting Information

This contains a detailed Experimental Section, thermoanalytical Mössbauer and Raman data, AC magnetic measurements, magnetic fitting, and crystallographic information (CIF data). This material is available free of charge via the Internet at http://pubs.acs.org.

AUTHOR INFORMATION

Corresponding Author

*E-mail: depedrovm@unican.es.

Notes

The authors declare no competing financial interest.

■ ACKNOWLEDGMENTS

Financial support from the Spanish Ministerio de Ciencia e Innovación (Projects MAT2011-27573-C04 and FIS2012-37549-C05-04) and Becas Iberoamericas Jóvenes Profesores Investigadores, 2011, Santander Universidades is acknowledged. The authors gratefully acknowledge the computer resources, technical expertise, and assistance provided by the Red Española de Supercomputación and MALTA Consolider Ingenio 2010 (Ref. CSD2007-00045). The paper is (partly) based on the results of experiments carried out at the Swiss Spallation Neutron Source SINQ, Paul Scherrer Institut, Villigen, Switzerland and Institute Laue-Langevin (ILL) of Grenoble.

■ REFERENCES

(1) (a) Hagrman, P. J.; Hagrman, D.; Zubieta, J. *Angew. Chem., Int. Ed.* **1999**, *38*, 2638−2684. (b) Kickelbick, G. *Hybrid Materials;* Wiley.com: Hoboken, NJ, 2007.
(2) (a) Gomez-Romero, P. *Adv. Mater.* **2001**, *13*, 5. (b) Kitagawa, S.; Kitaura, R.; Noro, S.-i. *Angew. Chem., Int. Ed.* **2004**, *43*, 2334−2375.
(3) Giernoth, R. *Angew. Chem., Int. Ed.* **2010**, *49*, 2834−2839.
(4) Welton, T. *Chem. Rev.* **1999**, *99*, 2071−2084.
(5) Brown, P.; Butts, C. P.; Eastoe, J.; Padron Hernandez, E.; Machado, F. L. d. A.; de Oliveira, R. J. *Chem. Commun.* **2013**, *49*, 2765−2767.
(6) Mallick, B.; Balke, B.; Felser, C.; Mudring, A.-V. *Angew. Chem., Int. Ed.* **2008**, *47*, 7635−7638.
(7) Wang, H.; Yan, R.; Li, Z.; Zhang, X.; Zhang, S. *Catal. Commun.* **2010**, *11*, 763−767.
(8) (a) Brown, P.; Bushmelev, A.; Butts, C. P.; Cheng, J.; Eastoe, J.; Grillo, I.; Heenan, R. K.; Schmidt, A. M. *Angew. Chem., Int. Ed.* **2012**, *51*, 2414−2416. (b) Okuhata, M.; Funasako, Y.; Takahashi, K.; Mochida, T. *Chem. Commun.* **2013**, *49*, 7662−7664. (c) Hu, X. L.; Qian, L. W.; Tang, Y. M.; Guan, P. *Adv. Mater. Res.* **2013**, *702*, 74−78.
(9) Del Sesto, R. E.; McCleskey, T. M.; Burrell, A. K.; Baker, G. A.; Thompson, J. D.; Scott, B. L.; Wilkes, J. S.; Williams, P. *Chem. Commun.* **2008**, *0*, 447−449.
(10) Peppel, T.; Köckerling, M.; Geppert-Rybczyńska, M.; Ralys, R. V.; Lehmann, J. K.; Verevkin, S. P.; Heintz, A. *Angew. Chem., Int. Ed.* **2010**, *49*, 7116−7119.
(11) Bwambok, D. K.; Thuo, M. M.; Atkinson, M. B.; Mirica, K. A.; Shapiro, N. D.; Whitesides, G. M. *Anal. Chem.* **2013**, *85*, 8442−8447.
(12) Tanaka, K.; Ishiguro, F.; Chujo, Y. *J. Am. Chem. Soc.* **2010**, *132*, 17649−17651.
(13) Miao, C.-X.; Wang, J.-Q.; Yu, B.; Cheng, W.-G.; Sun, J.; Chanfreau, S.; He, L.-N.; Zhang, S.-J. *Chem. Commun.* **2011**, *47*, 2697−2699.
(14) Okuno, M.; Hamaguchi, H.; Hayashi, S. *Appl. Phys. Lett.* **2006**, *89*, 132506.
(15) (a) Santos, E.; Albo, J.; Rosatella, A.; Afonso, C. A. M.; Irabien, Á. *J. Chem. Technol. Biotechnol.* **2014**, *89*, 866−871. (b) Albo, J.; Santos, E.; Neves, L. A.; Simeonov, S. P.; Afonso, C. A. M.; Crespo, J. G.; Irabien, A. *Sep. Purif. Technol.* **2012**, *97*, 26−33.
(16) Mohammad Fauzi, A. H.; Amin, N. A. S.; Mat, R. *Appl. Energy* **2014**, *114*, 809−818.
(17) Steed, J. W.; Atwood, J. L. *Supramolecular Chemistry;* John Wiley & Sons: Hoboken, NJ, 2009.
(18) (a) Weingärtner, H. *Angew. Chem., Int. Ed.* **2008**, *47*, 654−670. (b) Dupont, J. *J. Braz. Chem. Soc.* **2004**, *15*, 341−350.
(19) Estager, J.; Holbrey, J.; Swadźba-Kwaśny, M. *Chem. Soc. Rev.* **2014**, *43*, 847−886.
(20) Bertani, R.; Sgarbossa, P.; Venzo, A.; Lelj, F.; Amati, M.; Resnati, G.; Pilati, T.; Metrangolo, P.; Terraneo, G. *Coord. Chem. Rev.* **2010**, *254*, 677−695.
(21) Frontera, A.; Gamez, P.; Mascal, M.; Mooibroek, T. J.; Reedijk, J. *Angew. Chem., Int. Ed.* **2011**, *50*, 9564−9583.
(22) Estarellas, C.; Quiñonero, D.; Deyà, P. M.; Frontera, A. *ChemPhysChem* **2013**, *14*, 145−154.
(23) (a) Metrangolo, P.; Neukirch, H.; Pilati, T.; Resnati, G. *Acc. Chem. Res.* **2005**, *38*, 386−395. (b) Lommerse, J. P.; Stone, A. J.; Taylor, R.; Allen, F. H. *J. Am. Chem. Soc.* **1996**, *118*, 3108−3116.
(24) (a) Ouahab, L.; Enoki, T. *Eur. J. Inorg. Chem.* **2004**, *2004*, 933−941. (b) Coronado, E.; Day, P. *Chem. Rev.* **2004**, *104*, 5419−5448. (c) Kobayashi, H.; Cui, H.; Kobayashi, A. *Chem. Rev.* **2004**, *104*, 5265−5288.
(25) Enoki, T.; Miyazaki, A. *Chem. Rev.* **2004**, *104*, 5449−5478.
(26) (a) Yoshida, Y.; Otsuka, A.; Saito, G.; Natsume, S.; Nishibori, E.; Takata, M.; Sakata, M.; Takahashi, M.; Yoko, T. *Bull. Chem. Soc. Jpn.* **2005**, *78*, 1921−1928. (b) Yoshida, Y.; Saito, G. *J. Mater. Chem.* **2006**, *16*, 1254−1262. (c) de Pedro, I.; Rojas, D. P.; Albo, J.; Luis, P.; Irabien, A.; Blanco, J. A.; Rodriguez Fernandez, J. *J. Phys.: Condens. Matter* **2010**, *22*, 296006. (d) de Pedro, I.; Rojas, D. P.; Blanco, J. A.; Rodriguez Fernandez, J. *J. Magn. Magn. Mater.* **2011**, *323*, 1254−1257.
(27) (a) Bäcker, T.; Breunig, O.; Valldor, M.; Merz, K.; Vasylyeva, V.; Mudring, A.-V. *Cryst. Growth Des.* **2011**, *11*, 2564−2571. (b) Lin, I. J.; Vasam, C. S. *J. Organomet. Chem.* **2005**, *690*, 3498−3512.
(28) Hayashi, S.; Hamaguchi, H.-O. *Chem. Lett.* **2004**, *33*, 1590−1591.
(29) García-Saiz, A.; Migowski, P.; Vallcorba, O.; Junquera, J.; Blanco, J. A.; González, J. A.; Fernández-Díaz, M. T.; Rius, J.; Dupont, J.; Rodríguez Fernández, J.; de Pedro, I. *Chem.—Eur. J.* **2014**, *20*, 72−76.
(30) Soler, J. M.; Artacho, E.; Gale, J. D.; García, A.; Junquera, J.; Ordejón, P.; Sánchez-Portal, D. *J. Phys.: Condens. Matter* **2002**, *14*, 2745−2779.
(31) Román-Pérez, G.; Soler, J. M. *Phys. Rev. Lett.* **2009**, *103*, 096102.
(32) Dion, M.; Rydberg, H.; Schröder, E.; Langreth, D. C.; Lundqvist, B. I. *Phys. Rev. Lett.* **2004**, *92*, 246401.
(33) Kohanoff, J.; Pinilla, C.; Youngs, T. G.; Artacho, E.; Soler, J. M. *J. Chem. Phys.* **2011**, *135*, 154505.
(34) Zhong, C.; Sasaki, T.; Jimbo-Kobayashi, A.; Fujiwara, E.; Kobayashi, A.; Tada, M.; Iwasawa, Y. *Bull. Chem. Soc. Jpn.* **2007**, *80*, 2365−2374.
(35) Salonen, L. M.; Ellermann, M.; Diederich, F. *Angew. Chem., Int. Ed.* **2011**, *50*, 4808−4842.
(36) Arunan, E.; Desiraju, G. R.; Klein, R. A.; Sadlej, J.; Scheiner, S.; Alkorta, I.; Clary, D. C.; Crabtree, R. H.; Dannenberg, J. J.; Hobza, P.; Kjaergaard, H. G.; Legon, A. C.; Mennucci, B.; Nesbitt, D. J. *Pure Appl. Chem.* **2011**, *83*, 1637−1641.
(37) (a) Roth, C.; Peppel, T.; Fumino, K.; Kockerling, M.; Ludwig, R. *Angew. Chem., Int. Ed.* **2010**, *49*, 10221−10224. (b) Wulf, A.; Fumino, K.; Ludwig, R. *Angew. Chem., Int. Ed.* **2010**, *49*, 449−453.
(38) Skarmoutsos, I.; Dellis, D.; Matthews, R. P.; Welton, T.; Hunt, P. A. *J. Phys. Chem. B* **2012**, *116*, 4921−4933.
(39) Matsumoto, K.; Hagiwara, R.; Mazej, Z.; Benkič, P.; Žemva, B. *Solid State Sci.* **2006**, *8*, 1250−1257.
(40) Hay, B. P.; Custelcean, R. *Cryst. Growth Des.* **2009**, *9*, 2539−2545.
(41) Estager, J.; Holbrey, J.; Swadźba-Kwaśny, M. *Chem. Soc. Rev.* **2014**, *43*, 847−886.
(42) Heimer, N. E.; Del Sesto, R. E.; Meng, Z.; Wilkes, J. S.; Carper, W. R. *J. Mol. Liq.* **2006**, *124*, 84−95.
(43) (a) Krieger, B. M.; Lee, H. Y.; Emge, T. J.; Wishart, J. F.; Castner, E. W., Jr. *Phys. Chem. Chem. Phys.* **2010**, *12*, 8919−8925. (b) Larkin, P. *Infrared and Raman Spectroscopy; Principles and Spectral Interpretation;* Elsevier: Amsterdam, The Netherlands, 2011. (c) Nyquist, R. A.; Kagel, R. O. *Handbook of Infrared and Raman Spectra of Inorganic Compounds and Organic Salts: Infrared Spectra of Inorganic Compounds;* Academic Press: Waltham, MA, 1972; Vol. 4.
(44) Nakamoto, K. *Infrared and Raman Spectra of Inorganic and Coordination Compounds;* Wiley Online Library: Hoboken, NJ, 1978.
(45) de Pedro, I.; Garcia-Saiz, A.; Gonzalez, J. A.; Ruiz de Larramendi, I.; Rojo, T.; Afonso, C.; Simeonov, S.; Waerenborgh, J. C.; Blanco, J. A.; Rodriguez, J. *Phys. Chem. Chem. Phys.* **2013**, *15*, 12724−12733.

(46) Clausen, C. A.; Good, M. L. *Inorg. Chem.* **1970**, *9*, 220−223.
(47) White, R.; Nemanich, R.; Herring, C. *Phys. Rev. B* **1982**, *25*, 1822.
(48) Abrashev, M.; Bäckström, J.; Börjesson, L.; Popov, V.; Chakalov, R.; Kolev, N.; Meng, R.-L.; Iliev, M. *Phys. Rev. B* **2002**, *65*, 184301.
(49) (a) Blumberg, G.; Abbamonte, P.; Klein, M.; Lee, W.; Ginsberg, D.; Miller, L.; Zibold, A. *Phys. Rev. B* **1996**, *53*, R11930. (b) Massey, M.; Baier, U.; Merlin, R.; Weber, W. *Phys. Rev. B* **1990**, *41*, 7822.
(50) Boca, R. *A Handbook of Magnetochemical Formulae;* Elsevier: Amsterdam, The Netherlands, 2012; p 1010.
(51) (a) Zora, J. A.; Seddon, K. R.; Hitchcock, P. B.; Lowe, C. B.; Shum, D. P.; Carlin, R. L. *Inorg. Chem.* **1990**, *29*, 3302−3308. (b) Campo, J.; Luzón, J.; Palacio, F.; McIntyre, G. J.; Millán, A.; Wildes, A. R. *Phys. Rev. B* **2008**, *78*, 054415.
(52) Hagrman, P. J.; Hagrman, D.; Zubieta, J. *Angew. Chem., Int. Ed.* **1999**, *38*, 2638−2684.
(53) García-Saiz, A.; de Pedro, I.; Blanco, J. A.; González, J.; Fernández, J. R. *J. Phys. Chem. B* **2013**, *117*, 3198−3206.
(54) (a) de Pedro, I.; Maria Rojo, J.; Luis Pizarro, J.; Rodriguez Fernandez, J.; Sanchez Marcos, J.; Teresa Fernandez-Diaz, M.; Arriortua, M.; Rojo, T. *J. Mater. Chem.* **2007**, *17*, 3915−3926. (b) de Pedro, I.; Rojo, J. M.; Jubera, V.; Fernandez, J. R.; Marcos, J. S.; Lezama, L.; Rojo, T. *J. Mater. Chem.* **2004**, *14*, 1157−1163.
(55) Dulong, P. L.; Petit, A. T. *Ann. Chim. Phys.* **1819**, *10*.
(56) (a) de Pedro, I.; Rojo, J. M.; Rodríguez Fernández, J.; Fernández-Díaz, M. T.; Rojo, T. *Phys. Rev. B* **2010**, *81*, 134431. (b) de Pedro, I.; Rojo, J. M.; Rodriguez Fernandez, J.; Sanchez Marcos, J.; Fernandez-Diaz, M. T.; Rojo, T. *J. Solid State Chem.* **2012**, *188*, 1−10.
(57) Debye, P. *Ann. Phys.* **1912**, *344*, 789−839.
(58) Blanco, J.; Gignoux, D.; Morin, P.; Schmitt, D. *J. Magn. Magn. Mater.* **1990**, *90*, 166−168.
(59) de Pedro, I.; Rojo, J. M.; Rius, J.; Vallcorba, O.; Ruiz de Larramendi, I.; Rodriguez Fernandez, J.; Lezama, L.; Rojo, T. *Inorg. Chem.* **2012**, *51*, 5246−5256.
(60) (a) Lautenschläger, G.; Weitzel, H.; Vogt, T.; Hock, R.; Böhm, A.; Bonnet, M.; Fuess, H. *Phys. Rev. B* **1993**, *48*, 6087−6098. (b) Boehm, M.; Roessli, B.; Schefer, J.; Wills, A. S.; Ouladdiaf, B.; Lelièvre-Berna, E.; Staub, U.; Petrakovskii, G. A. *Phys. Rev. B* **2003**, *68*, 024405.
(61) (a) Arquès, P.-Y. *J. Phys. (Paris)* **1971**, *32*, 1−5. (b) Rodríguez-Carvajal, J. *Phys. B* **1993**, *192*, 55−69.
(62) Blanco, J. A.; Espeso, J. I.; García Soldevilla, J.; Gómez Sal, J. C.; Ibarra, M. R.; Marquina, C.; Fischer, H. E. *Phys. Rev. B* **1999**, *59*, 512−518.
(63) Rosokha, Y. S.; Lindeman, S. V.; Rosokha, S. V.; Kochi, J. K. *Angew. Chem., Int. Ed.* **2004**, *43*, 4650−4652.
(64) Gamez, P.; Mooibroek, T. J.; Teat, S. J.; Reedijk, J. *Acc. Chem. Res.* **2007**, *40*, 435−444.
(65) Chun, Y.; Jiten Singh, N.; Hwang, I.-C.; Woo Lee, J.; Yu, S. U.; Kim, K. S. *Nat. Commun.* **2013**, *4*, 1797.
(66) Schottel, B. L.; Chifotides, H. T.; Dunbar, K. R. *Chem. Soc. Rev.* **2008**, *37*, 68−83.
(67) Leslie, M.; Gillan, N. *J. Phys. C: Solid State Phys.* **1985**, *18*, 973.
(68) Makov, G.; Payne, M. *Phys. Rev. B* **1995**, *51*, 4014.
(69) (a) Awwadi, F.; Haddad, S. F.; Willett, R. D.; Twamley, B. *Cryst. Growth Des.* **2009**, *10*, 158−164. (b) Jornet-Somoza, J.; Codina-Castillo, N.; Deumal, M.; Mota, F.; Novoa, J. J.; Butcher, R. T.; Turnbull, M. M.; Keith, B.; Landee, C. P.; Wikaira, J. L. *Inorg. Chem.* **2012**, *51*, 6315−6325. (c) Awwadi, F.; Willett, R. D.; Twamley, B.; Schneider, R.; Landee, C. P. *Inorg. Chem.* **2008**, *47*, 9327−9332. (d) Borrás-Almenar, J. J.; Coronado, E.; Müller, A.; Pope, M. *Polyoxometalate Molecular Science;* Springer: New York, 2003; Vol. *98*.
(70) (a) Kurmoo, M.; Day, P.; Guionneau, P.; Bravic, G.; Chasseau, D.; Ducasse, L.; Allan, M. L.; Marsden, I. D.; Friend, R. H. *Inorg. Chem.* **1996**, *35*, 4719−4726. (b) Zhang, B.; Wang, Z.; Fujiwara, H.; Kobayashi, H.; Kurmoo, M.; Inoue, K.; Mori, T.; Gao, S.; Zhang, Y.; Zhu, D. *Adv. Mater.* **2005**, *17*, 1988−1991.
(71) Turnbull, M. M.; Landee, C. P.; Wells, B. M. *Coord. Chem. Rev.* **2005**, *249*, 2567−2576.
(72) Awwadi, F. F.; Willett, R. D.; Peterson, K. A.; Twamley, B. *Chem.—Eur. J.* **2006**, *12*, 8952−8960.
(73) Glerup, J.; Goodson, P. A.; Hodgson, D. J.; Michelsen, K. *Inorg. Chem.* **1995**, *34*, 6255−6264.
(74) McElearney, J.; Merchant, S.; Carlin, R. *Inorg. Chem.* **1973**, *12*, 906−908.
(75) (a) Bonner, J. C.; Fisher, M. E. *Phys. Rev.* **1964**, *135*, A640−A658. (b) Kahn, O. *Molecular Magnetism;* VCH: New York, 1993; Vol. *60*.